Fire Safety Journal 106 (2019) 88–93

Contents lists available at ScienceDirect

Fire Safety Journal

journal homepage: www.elsevier.com/locate/firesaf

Fire ember pyrometry using a color camera

Dennis K. Kim, Peter B. Sunderland*

Dept. of Fire Protection Engineering, University of Maryland, College Park, MD, 20742, USA

ARTICLE INFO

Keywords:
Ash transmittance
Emissivity
Firebrand
Smoldering
Temperature
Wildland fire

ABSTRACT

Firebrands can dramatically increase the hazards of wildland fires. While embers have been extensively studied, little is known about their temperatures. To address this an imaging ember pyrometer is developed here using an inexpensive digital color camera. The camera response was calibrated with a blackbody furnace at 600–1200 °C. The embers were smoldering cylindrical maple rods, 6.4 mm in diameter and 2 cm long. Temperatures were obtained from ratios of green/red pixel values and from grayscale pixel values. Ratio pyrometry is more accurate when ember emissivity times ash transmittance is below unity, but grayscale pyrometry has signal-to-noise ratios 18 times as high. Thus a hybrid pyrometer was developed that has the advantages of both, providing a spatial resolution of 17 μm, a signal-to-noise ratio of 530, and an estimated uncertainty of ± 20 °C. The measured ember temperatures were between 750 and 1070 °C with a mean of 930 °C. Comparing the ratio and grayscale temperatures indicates the ember's mean emissivity times ash transmittance in the visible was 0.73. Temperatures were also measured with fine bare-wire thermocouples, which were found to underpredict the ember's mean temperature by 230 °C owing to ember quenching and imperfect thermal contact.

1. Introduction

Wildland fires are a problem with global impact. They are responsible for increasing losses of lives and property, and increasing costs of fire prevention and suppression [1,2]. Of particular concern are fires in the wildland-urban interface [3].

Embers are smoldering fuels, and firebrands are airborne embers. Firebrands can have a large impact on wildland fire spread [4,5] and they often complicate firefighting [6]. Firebrands can be lofted several km and still ignite spot fires. An improved understanding of firebrands is crucial to protecting against wildland fires, e.g., by contributing to improved fire codes and standards, improved vegetation management, and improved computational fire models.

Extensive research has been conducted on embers and firebrands, examining firebrand mass and morphology [7,8], generation [8–10], transport [11–13], and viability to ignite spot fires [7,14,15]. Firebrand behavior has been simulated using geometric scaling, analytical models, and numerical models [10–13].

Much less is known about ember temperatures. This could be impeding fire safety because cool firebrands are not viable ignition sources and may be incapable of self-sustained burning, whereas hot and small firebrands have short burning durations. Measurements have been performed with thermocouples [14,16], but these suffer from smolder quenching and poor thermal contact.

Ember pyrometry has been performed with infrared (IR) imagers and IR spot detectors. Temperatures of 190–946 °C have been reported [4,6,14,17]. However, these diagnostics have several drawbacks: the surface emissivity, ε, and the transmittance of ash and/or smoke along the line of sight, τ, must be known or estimated [4,14,16] and an isothermal region of the ember must fill each pixel or the spot detector. Compared to modern color cameras, IR imagers have high costs and low pixel counts. For example, the IR imager used by Ref. [4] for ember pyrometry (FLIR Model A8300sc) costs US$ 100,000 but has just 0.9 megapixels.

Consumer-grade color cameras have been used extensively to perform ratio pyrometry of soot [18–22]. More recently, this has been used for surface pyrometry. Lu et al. [23] measured temperatures of embers burning inside flow reactors with wall temperatures above 1000 °C. Similar measurements were performed for burning coal particles [24,25]. None of these studies considered self-sustaining combustion like that of a firebrand. Ratio pyrometry has been applied to heated materials at 500–1930 °C [26–28], but the materials were not flammable. During the final round of reviews for this paper, two related papers were published [29,30].

A nonintrusive and inexpensive ember pyrometer is developed here using a color camera. By combining ratio and grayscale pyrometry, a hybrid pyrometer is developed that incorporates the accuracy of ratio pyrometry and the low noise of grayscale pyrometry. The

* Corresponding author. University of Maryland, Dept. of Fire Protection Engineering, 3104 J.M. Patterson Building, College Park, MD, 20742, USA.
E-mail address: pbs@umd.edu (P.B. Sunderland).

https://doi.org/10.1016/j.firesaf.2019.04.006
Received 22 October 2018; Received in revised form 7 February 2019; Accepted 16 April 2019
Available online 17 April 2019

measurements also yield the product $\varepsilon\,\tau$ in the visible.

2. Experimental

The fuel was cylindrical maple rods, 6.4 mm in diameter (McMaster Carr). These were cut 20 mm long and 3.2 mm axial holes were drilled to promote burning. Maple rods were observed to burn more steadily than oak or birch rods. Prior to ignition the rods were dried for 3 h in an oven at 103 °C [31]. SiC yarn, 0.5 mm in diameter, was inserted into the holes for mounting. No effect of ember cooling by the yarn was detected. The rods were mounted horizontally. The terminal velocity of such a rod (neglecting its hole) with its axis horizontal in air at 25 °C and 1.01 bar is 12 m/s [32].

For some tests a thermocouple was used. For this a circumferential groove with a width of 0.5 mm was cut in the rod. A bare-wire K-type thermocouple with a wire diameter of 125 µm was placed into the groove. Tension was applied such that the bead remained in contact with the rod. The thermocouple output was recorded at a sampling rate of 2 kHz. No corrections were made for thermocouple radiation or conduction.

A 50 mm long laminar diffusion flame from a laminar butane diffusion flame was used for ignition. The flame tip impinged on the bottom of the rod, translated back and forth across its length for 8 s, and was removed. Time zero was defined as the onset of flame impingement.

The ember supported flaming combustion until approximately 35 s. A fan above the camera was activated at 40 s to promote uniform smoldering on the ember surface. The fan discharge was at an angle of 30° below horizontal, producing an air velocity near the firebrand of 2.5 m/s (determined with a handheld rotating vane anemometer.) At approximately 70 s, the rod began to break up and fall from its mount. Little or no smoke was observed. Small amounts of gray ash accumulated on the ember and then fell away.

Imaging was performed with a Sony DSC-RX10 III cyber-shot digital camera. This has a 1.3 × 0.9 cm Exmor RS stacked back-illuminated complementary metal-oxide semiconductor (CMOS) sensor with 20.1 megapixels and a bit depth of 14 in each color plane. The lens was a Zeiss Vario-Sonnar T* Lens, with variable zoom (8.8–220 mm) and *f* (2.4–4). A Hoya 72 mm protector filter was attached to the lens to facilitate cleaning.

Although BG7 colored glass filters [22,33] or interference bandpass filters [20,34] are common in soot pyrometry, no filters were used here so the transient burning could be observed with the shortest exposure times. For example, images of the blackbody furnace at 1000 °C with a BG7 filter required a factor of 60 increase in exposure time to obtain comparable grayscale pixel values.

To avoid rolling shutter distortions only the mechanical shutter was used. The white balance was daylight, but this had no effect because the images were recorded in RAW format. The *ISO* (International Organization for Standardization) range was 100–400, which for this camera controls the electronic gain, rather than image postprocessing.

The RAW images were converted to 16 bit tiff images using dcraw [35] with default settings except −4 and –T [20]. The tiff files were opened in ImageJ. Rectangular regions were selected and for these the pixel coordinates and the red, green, and blue pixel values (I_R, I_G, and I_B) were exported. Saturation occurred at a pixel value of 65535. Dark images were recorded at various shutter times to determine the dark-current pixel values, I_{DC}, but these were small (below 50 in each color plane) and had a negligible variation with shutter time.

Grayscale pixel values were defined as

$$I_{GS} = (I_R + I_G + I_B)\,/\,3 \tag{1}$$

and normalized pixel values were defined as

$$NI_i = (I_i - I_{i,DC})\,f^{\,2}\,/\,(t\ ISO) \tag{2}$$

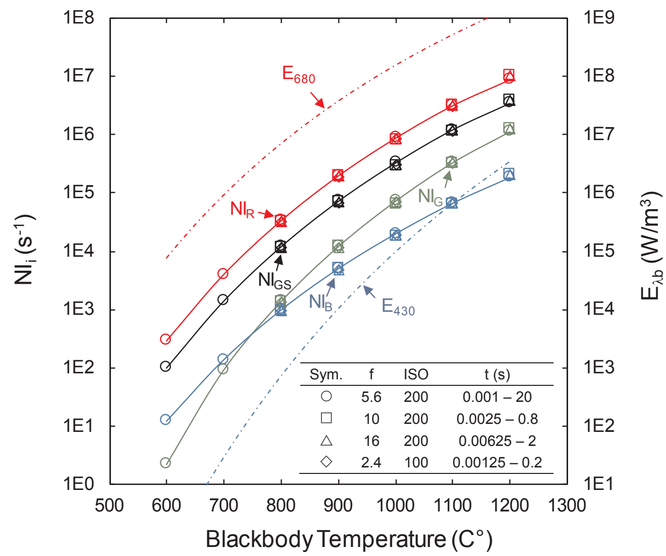

Fig. 1. Measured normalized pixel values of the blackbody furnace images. Also shown is the blackbody spectral emissive power at 430 and 680 nm.

where *f* is f-number, *i* denotes *R, G, B*, or *GS*, and *t* is exposure time.

3. Camera calibration

The camera was calibrated with a blackbody furnace (Oriel 67032). It has a maximum temperature of 1200 °C, a temperature accuracy of ± 0.2 °C, an emissivity of $\varepsilon = 0.99 \pm 0.01$, and an aperture diameter of 25 mm. A similar blackbody was found to have $\varepsilon = 0.99$ for wavelengths between 0.5 and 4 µm [36]. The lens was 1 cm away and was focused on the aperture. Exposure times were adjusted such that the highest pixel values (always red) were close to saturation but none was saturated.

For each image a 200 × 200 pixel region centered on the middle of the aperture was selected, this corresponding to about 5% of the aperture. For this region, the mean normalized pixel values are plotted with respect to blackbody temperature in Fig. 1. The normalization of Eq. (2) is seen to collapse the measurements for various *f*, *ISO*, and *t*. There is a 4–5 order of magnitude increase in *NI* as blackbody temperature increases from 600 to 1200 °C. The red pixel values are the highest, and those for green are higher than for blue except at low temperatures. Additional tests (not included in Fig. 1) found these correlations to be independent of both lens zoom and distance from the blackbody.

The spectral emissive power of a blackbody is

$$E_{\lambda b} = C_1\,/\,\{\,\lambda^5\,[\,\exp\,(C_2\,/\,\lambda\,T) - 1\,]\,\} \tag{3}$$

where C_1, C_2, T, and λ are, respectively, first and second radiation constants (3.742×10^{-16} W-m^2 and 0.01439 m-K), temperature, and wavelength. Quantity $E_{\lambda b}$ is plotted in Fig. 1 at 430 and 680 nm, which are close to the peak sensitivities of similar cameras in the blue and red planes [27,35,37]. Among the six curves in Fig. 1, five have similar shapes. However, the NI_B curve has a smaller slope owing to the behavior of the CMOS and/or its filter mask.

The *NI* correlations in Fig. 1 allow pyrometry on hot objects such as smoldering embers. This can be ratio pyrometry, based on one or more *NI* ratios, or grayscale pyrometry, based on NI_{GS}. Ratio pyrometry has lower signal-to-noise ratios (SNRs). On the other hand, grayscale pyrometry generally requires: blackbody behavior of the hot surface; negligible radiative extinction from ash and smoke; and no temporal drift or ambient temperature dependence in the camera.

For ratio pyrometry the three *NI* of Fig. 1 are converted to three ratios as plotted in Fig. 2. These are smooth and monotonic with respect

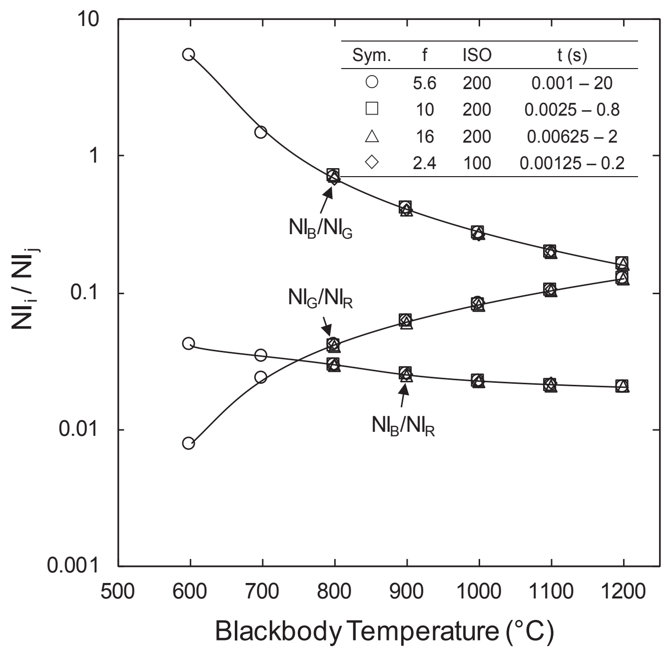

Fig. 2. Normalized pixel value ratios of the blackbody furnace images.

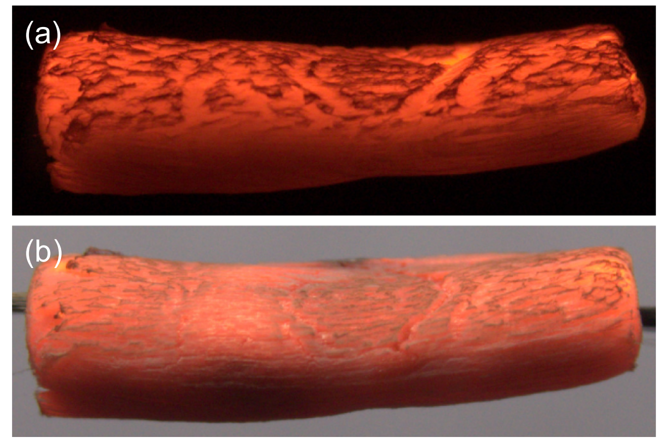

Fig. 3. Representative color images (1212 × 396 pixels) of a glowing ember (a) with no external illumination; and (b) with a lamp behind the camera. For both images $ISO = 400$, $f = 2.8$, and $t = 1.56$ ms. For improved visualization, some pixels are saturated.

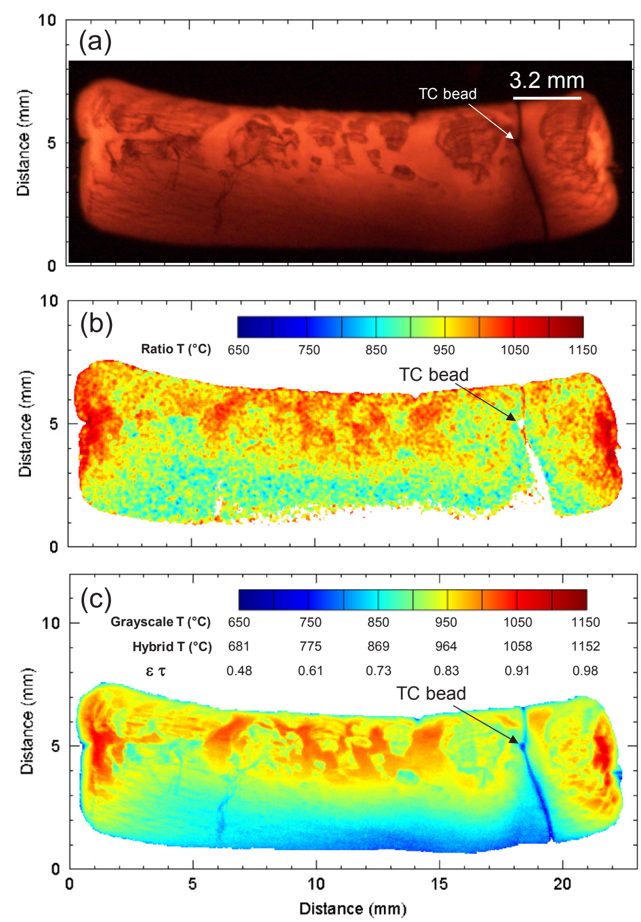

Fig. 4. (a) Representative color image (1200 × 432 pixels) of a smoldering ember at 50 s. For this image $ISO = 200$, $f = 2.8$, and $t = 1.3$ ms. Figure (b) is the resulting color contour plot of ratio pyrometry temperatures. Figure (c) is the resulting color contour plot of: grayscale pyrometry temperatures, hybrid pyrometry temperatures, and visible emissivity times ash transmittance.

to temperature. A camera whose red, green, and blue planes had no wavelength overlap would yield a monotonic increase in these ratios with increasing temperature. Such monotonicity has been observed before for some cameras [33,37], but not for others [23,28,38]. It is seen in Fig. 2 only for G/R. Both ratios involving the blue color plane decrease with temperature owing to the low slope of NI_B evident in Fig. 1.

The B/R curve in Fig. 2 is too flat for ratio pyrometry with reasonable signal-to-noise ratios. B/G ratio pyrometry was found to yield unacceptably high scatter because it omits the red pixels, which have the highest pixel values and the highest signal-to-noise ratios. Thus, only G/R is considered below for ratio pyrometry.

The variation in NI_G/NI_R in Fig. 2 varies by only a factor of 16, indicating a decreased signal-to-noise ratio for ratio pyrometry as compared to grayscale pyrometry using Fig. 1. Pyrometry performed on the blackbody images indicated SNRs (the temperature mean divided by standard deviation) of 30 and 530 for ratio and grayscale pyrometry, respectively. These values vary by a factor of 18.

4. Ember pyrometry

Pyrometry was performed on smoldering embers. For this the camera was mounted with its optical axis horizontal and perpendicular to an ember. The front of the lens was 1 cm from the closest part of the ember and the zoom setting was 11.5 mm. The focus was adjusted to be clear across as much of the ember surface as possible.

An image of a smoldering ember without external illumination is shown in Fig. 3a. This was recorded 40 s after ignition. The initial cross section of the ember was a rectangle, but it deformed during burning. The bottom of the ember is relatively dim owing to the downward fan orientation. The top of the ember is mostly orange, but has many raised black regions.

The image of Fig. 3b was recorded 6 s earlier with a lamp behind the camera. This illumination changes the black regions to light gray, indicating they are ash. This identification of ash was confirmed by scratching ember surfaces with a small blade, whereby gray ash fell away and the black regions became orange.

For ember pyrometry, images similar to Fig. 3a were recorded with dimmer exposures such that the pixel values were as high as possible without saturation at any pixel in any color plane. One such image is shown in Fig. 4a. The size of each pixel in the object plane is 17 μm. The thermocouple (TC) is visible as the dark vertical band and its bead location is indicated in Fig. 4.

For ratio pyrometry, NI_G/NI_R was found for each pixel in Fig. 4a. These were converted to temperatures using the curve fit of Fig. 2, a 3rd order best-fit polynomial of T in terms of $\log(NI_G/NI_R)$. A null temperature was assigned to every pixel that was outside the ember, had a green pixel value below 100, and/or was outside the range of 600–1200 °C. Owing to scatter, spatial smoothing was performed. For this, each pixel was assigned the mean temperature of the unsmoothed temperatures of the 7 × 7 pixel region centered on it. Pixels with a null temperature were excluded from this mean. If more than 50% of these 49 pixels had null temperatures, the smoothed center pixel was assigned a null temperature.

Fig. 4b shows the ratio pyrometry results. The hottest regions correspond to the orange regions in Fig. 4a. The coolest are near the ember bottom, where air velocities are low. The ends of the embers are hot owing to low heat conduction rates into the unburned wood. The black regions surrounded by orange, identified above as ash, are cool because the ash slows the transport of oxygen and products.

For grayscale pyrometry, NI_{GS} was found for each pixel in Fig. 4a. These were converted to temperatures using the curve fit of Fig. 1, a 2nd order best-fit polynomial of T in terms of $\log(NI_{GS})$. A null temperature was assigned to every pixel that was outside the ember or within 6 pixels of the ember edge. No pixel within the ember was outside the range of 600–1200 °C. No spatial smoothing was applied. Fig. 4c, with its first legend line, shows the grayscale pyrometry results. Compared to the ratio pyrometry results these temperatures are far less scattered. This is despite 7 × 7 pixel spatial smoothing in the ratio pyrometry and none in the grayscale pyrometry.

In Fig. 4b and c, grayscale pyrometry indicates lower temperatures than ratio pyrometry at most locations. The ratio pyrometer is immune from interference of nonunity emissivity times ash transmittance ($\varepsilon\ \tau$) when $\varepsilon\ \tau$ is the same for the R and G pixel wavelengths. The grayscale pyrometer has no such immunity, as it interprets decreased GS pixel values as decreased temperatures.

This behavior was investigated by comparing the mean temperatures of 30 × 30 pixel regions that were nearly isothermal for both ratio and grayscale pyrometry. Both ash-covered and ash-free regions were included. Several embers were considered, with various air velocities, and the results are plotted in Fig. 5. The grayscale pyrometry temperatures are generally cooler, and this difference decreases with increasing temperature. The measurements are well correlated with the line fit shown.

This correlation allows the grayscale pyrometry temperatures, with

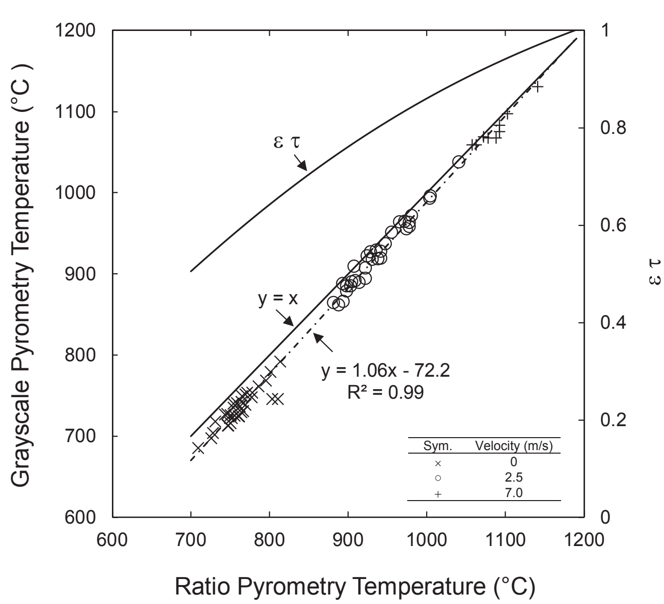

Fig. 5. Grayscale pyrometry temperature and visible emissivity plotted with respect to ratio pyrometry temperature for smoldering embers. For the 7 m/s tests the ratio pyrometry correlation was extrapolated to 1300 °C.

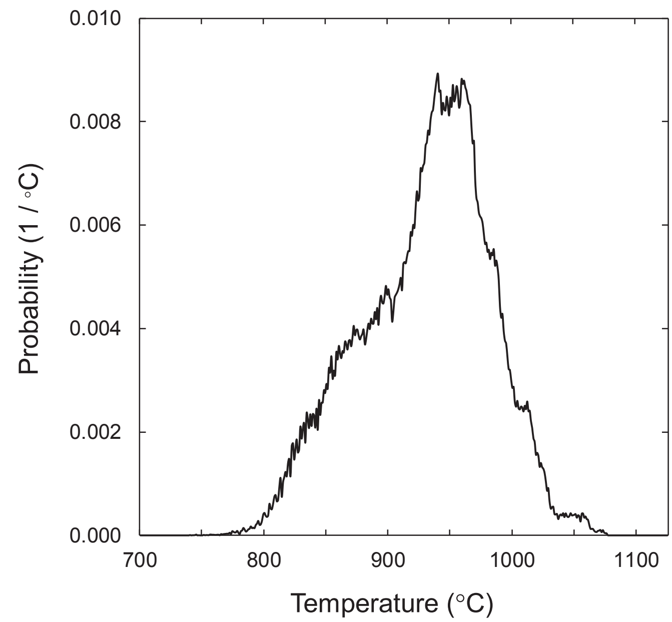

Fig. 6. PDF of the temperature of the ember of Fig. 4 using hybrid pyrometry. The bin width was 1 °C.

their low noise, to be corrected upward to match the ratio pyrometry results, with their resilience against nonunity $\varepsilon\ \tau$. This correction yields what is termed here hybrid pyrometry. From the correlation in Fig. 5, the hybrid pyrometry temperature is

$$T_{hybrid} = (T_{GS} + 72.2\,^{\circ}\mathrm{C}) / 1.06 \tag{4}$$

For the ember of Fig. 4a, the hybrid pyrometry results are shown in Fig. 4c using its second legend line.

Fig. 6 shows the probability density function (pdf) of the hybrid temperatures of Fig. 4c. Its shape is similar to pdfs of smoldering coal [25]. The mean temperature was 930 °C, and the standard deviation was 52 °C. The minimum and maximum temperatures (excluding the 20 coolest and 20 hottest pixels) were 750 and 1070 °C.

5. Visible emissivity times ash transmittance

For a smoldering ember with emissivity ε and with emission passing through ash and/or smoke with transmittance τ, the resulting spectral emissive power is

$$E_{\lambda} = \varepsilon\ \tau\ E_{\lambda b} \tag{5}$$

where $E_{\lambda b}$ is given by Eq. (3) and where ε and τ are evaluated at wavelength λ. Assuming the product $\varepsilon\ \tau$ is the same for the wavelengths recorded by the R and G pixels, the temperature indicated by ratio pyrometry, T_{ratio}, is the true temperature of the ember below the ash. The temperature indicated by grayscale pyrometry, T_{GS}, predicated on $\varepsilon = \tau = 1$, is the temperature of a blackbody with the same spectral emissive power for the wavelengths detected. Evaluating the right side of Eq. (5) at T_{ratio} and the right side of Eq. (3) at T_{GS} and equating them allows the product $\varepsilon\ \tau$ to be determined from

$$\varepsilon\ \tau = \exp\left[\,-\,C_2\,(T_{GS}^{\ -1} - T_{ratio}^{\ -1})\,/\,\lambda\,\right] \tag{6}$$

Because the red pixel values are the highest, Eq. (6) is evaluated here at $\lambda = 680$ nm. Equation (6), combined with the linear relationship between T_{GS} and T_{ratio} in Fig. 5, allows $\varepsilon\ \tau$ to be plotted with respect to T_{ratio} in Fig. 5. The product $\varepsilon\ \tau$ increases with temperature. This is consistent with emissivity measurements, which found it to increase with metal temperature [26] and with ember burn time [23].

Equations (4) and (6) allow $\varepsilon\ \tau$ to be estimated from T_{hybrid}. This is demonstrated in Fig. 4c using its third legend line. This ember has a

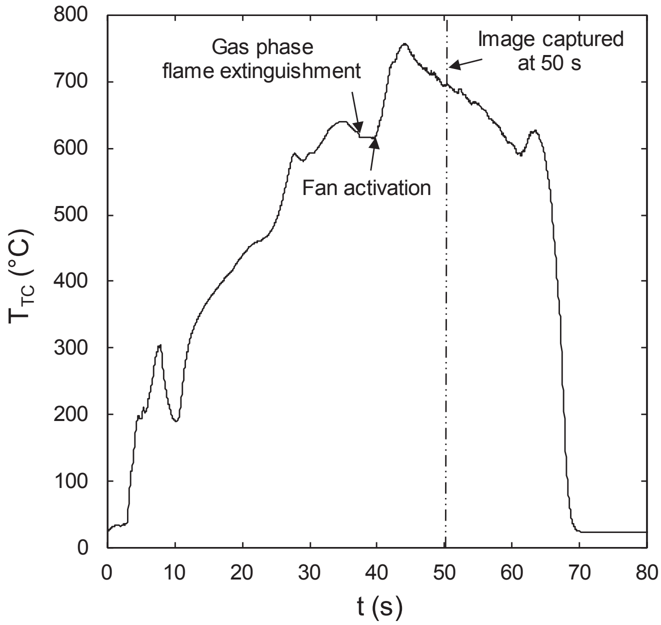

Fig. 7. Thermocouple temperature plotted with respect to time.

mean $\varepsilon\,\tau$ of 0.73. This is larger than the ember emissivity of 0.6 in the infrared reported by Ref. [14], but a direct comparison is difficult because the wavelengths are different.

The transmittance in the visible of a thin layer of ash on these embers can be estimated from this form of the Lambert-Beer Law,

$$\tau = \exp\left(-k_p\,\rho\,Y\,L\right) \tag{7}$$

where k_p is the ash mass extinction coefficient, L is the ash layer thickness, Y is the mass of ash per mass of wood burned, and ρ is the virgin wood density. Reference [39] reports $k_p = 0.229\ \mathrm{m^2/g}$ for coal ash in the visible. The measured density of the maple rods is 746 kg/m^3. Quantity Y for wood is estimated from Table 1 of Ref. [40] to be 5.8E-3. The ember images of Fig. 3 indicate an ash layer thickness of 0–0.3 mm. Inserting these values into Eq. (7) predicts a range of τ of 0.74–1. The uncertainties on this estimate are large owing to uncertainties in k_p and L.

Although smoke was occasionally seen above the ember, none was observed between the ember and the camera. Because both ash-free regions, with unity τ, and ash-covered regions follow the same correlation in Fig. 5, it is possible that the minimum τ of 0.74 estimated above is too low and that τ is nearly unity for this ember.

6. Thermocouple results

The thermocouple temperatures for the test of Fig. 4 are plotted in Fig. 7. When Fig. 4a was recorded the thermocouple temperature was 695 °C, which is 230 °C lower than the mean ember temperature determined by pyrometry. This suggests that past measurements of ember temperatures with thermocouples, with a reported range of 220–850 °C, may have been biased downward by a similar amount [14,16].

Grayscale and hybrid pyrometry performed on the image of the thermocouple bead indicated its temperature to be 757 and 781 °C, respectively. These temperatures are higher owing to imperfect imaging of the small bead. Hybrid pyrometry indicated a temperature of the smolder region near the bead of 860 °C. Fig. 4b and c shows that the thermocouple causes significant smolder quenching. Additionally, the thermocouple bead is cooler than the adjacent ember owing to imperfect thermal contact.

Representative blackbody images were used to estimate the pyrometer uncertainties. Pixels were chosen at random in the images, and their pixel values converted to T_{ratio} and T_{GS}. The means of these temperatures were within 3 °C of the blackbody temperature. The absolute value of the difference between these temperatures and the blackbody temperature had means of 23 and 4 °C for T_{ratio} and T_{GS} ratio, respectively. Owing to less uniform temperatures and uncertainties in $\varepsilon\,\tau$, for smoldering embers the uncertainty in T_{hybrid} at any pixel is estimated at ± 20 °C. A temperature difference of ± 20 °C would result if $\varepsilon\,\tau$ varies by ± 7% between green and red at 900 °C. The estimated uncertainty for $\varepsilon\,\tau$ is ± 10%.

It is expected that this pyrometer can be applied with similar uncertainty to embers of other materials and shapes and/or in environments with different compositions and flowfields. The main limitations are that the ember temperatures should be within the range of this calibration (600–1200 °C), and, while $\varepsilon\,\tau$ can vary with position, it should not be significantly different for the wavelengths recorded by the R and G pixels.

7. Conclusions

A digital color camera was used to perform pyrometry on smoldering wood embers. Calibration was with a blackbody furnace. The major findings are as follows.

1. Ratio pyrometry is accurate when the product $\varepsilon\,\tau$ is invariant across the detected wavelengths. Grayscale pyrometry is accurate when $\varepsilon\,\tau$ is unity, which is less common. The SNR for grayscale pyrometry is 18 times as high.
2. Grayscale pyrometry temperatures are lower and are linearly correlated with ratio pyrometry temperatures. This correlation allows hybrid pyrometry, whereby the grayscale temperatures are corrected upward to account for nonunity $\varepsilon\,\tau$. It also allows determinations of $\varepsilon\,\tau$.
3. The hybrid pyrometer had a spatial resolution of 17 µm, a SNR of 530, and an estimated uncertainty of ± 20 °C.
4. The measured ember temperatures were between 750 and 1070 °C with a mean of 930 °C. Ash and smoke caused negligible attenuation. The mean $\varepsilon\,\tau$ was 0.73.
5. Even fine bare-wire thermocouples quench smolder reactions and make imperfect thermal contact. For these tests the thermocouple indicated a temperature 230 °C below the mean ember temperature.

Declaration of interest

None. There are no financial or personal relationships with other people or organizations that could inappropriately influence (bias) this work.

Acknowledgments

This work was supported by NIST grant 70NANB17H212 with Nicolas Bouvet as technical contact. Eric Auth assisted with the image analysis.

References

[1] J.D. Cohen, Preventing disaster: home ignitability in the wildland urban interface, J. For. 98 (2000) 15–21.
[2] A. Sharifian, J. Hashempour, A novel ember shower simulator for assessing performance of low porosity screens at high wind speeds against firebrand attacks, J. Fire Sci. 34 (2016) 335–355.
[3] W.E. Mell, S.L. Manzello, A. Maranghides, D. Butry, R.G. Rehm, The wildland-urban interface fire problem – current approaches and research needs, Int. J. Wildland Fire 19 (2010) 238–251.
[4] S.E. Caton, R.S.P. Hakes, D.J. Gorham, A. Zhou, M.J. Gollner, Review of pathways for building fire spread in the wildland urban interface part 1: exposure conditions, Fire Technol. 53 (2016) 429–473.
[5] J.L. Pellegrino, N.P. Bryner, E.L. Johnsson, Wildland-urban interface fire research needs: workshop summary report, NIST - Spec. Publ. 1150 (2013).
[6] C. He, K. Liu, L. Shu, X. Hong, S. Zhang, The diagnostic methods for resurgences of

smoldering fire in the forests by infrared thermal imaging, Spectrosc. Spectr. Anal. 38 (2018) 326–332.
[7] A. Ganteaume, M. Guijarro, M. Jappiot, C. Hernando, C. Lampin-Maillet, Pedro Perez-Gorostiaga, J.A. Vega, Laboratory characterization of firebrands involved in spot fires, Ann. For. Sci. 68 (2011) 531–541.
[8] S. Suzuki, E. Johnsson, A. Maranghides, S.L. Manzello, Ignition of wood fencing assemblies exposed to continuous wind-driven firebrand showers, Fire Technol. 52 (2016) 1051–1067.
[9] S.L. Manzello, J.R. Shields, T.G. Cleary, A. Maranghides, W.E. Mell, J.C. Yang, Y. Hayashi, D. Nii, T. Kurita, On the development and characterization of a firebrand generator, Fire Saf. J. 43 (2008) 258–268.
[10] A. Tohidi, N. Kaye, W. Bridges, Statistical description of firebrand size and shape distribution from coniferous trees for use in Metropolis Monte Carlo simulations of firebrand flight distance, Fire Saf. J. 77 (2015) 21–35.
[11] C.S. Tarifa, P. P Del Notario, F.G. Moreno, On the flight paths and lifetimes of burning particles of wood, Proc. Combust. Inst. 10 (1965) 1021–1037.
[12] R.A. Anthenien, S.D. Tse, A.C. Fernandez-Pello, On the trajectories of embers initially elevated or lofted by small scale ground fire plumes in high winds, Fire Saf. J. 41 (2006) 349–363.
[13] S.D. Tse, A.C. Fernandez-Pello, On the flight paths of metal particles and embers generated by power lines in high winds–a potential source of wildland fires, Fire Saf. J. 30 (1998) 333–356.
[14] S.L. Manzello, S. Park, T.G. Cleary, Investigation on the ability of glowing firebrands deposited within crevice to ignite common building materials, Fire Saf. J. 44 (2009) 894–900.
[15] S.L. Manzello, T.G. Cleary, J.R. Shields, J.C. Yang, Ignition of mulch and grasses by firebrands in wildland-urban interface fires, Int. J. Wildland Fire 15 (2006) 427–431.
[16] J. Urbas, W.J. Parker, G.E. Luebbers, Surface temperature measurements on burning materials using an infrared pyrometer: accounting for emissivity and reflection of external radiation, Fire Mater. 28 (2004) 33–53.
[17] V. Fateev, M. Agafontsev, S. Volkov, A. Filkov, Determination of smoldering time and thermal characteristics of firebrands under laboratory conditions, Fire Saf. J. 91 (2017) 791–799.
[18] D.L. Urban, Z.-G. Yuan, P.B. Sunderland, G.T. Linteris, J.E. Voss, K.-C. Lin, Z. Dai, K. Sun, G.M. Faeth, Structure and soot properties of nonbuoyant ethylene/air laminar jet diffusion flames, AIAA J. 36 (1998) 1346–1360.
[19] F.J. Diez, C. Aalburg, P.B. Sunderland, D.L. Urban, Z.-G. Yuan, G.M. Faeth, Soot properties of laminar jet diffusion flames in microgravity, Combust. Flame 156 (2009) 1514–1524.
[20] H. Guo, J.A. Castillo, P.B. Sunderland, Digital camera measurements of soot temperature and soot volume fraction in axisymmetric flames, Appl. Opt. 52 (2013) 8040–8047.
[21] M. Jakob, P. Lehnen, P. Adomeit, S. Pischinger, Development and application of a stereoscopic 3-color high-speed ratio-pyrometry, Combust. Flame 161 (2014) 2825–2841.
[22] D. Giassi, B. Liu, M.B. Long, Use of high dynamic range imaging for quantitative combustion diagnostics, Appl. Opt. 54 (2015) 4580–4588.
[23] H. Lu, L. Ip, A. Mackrory, L. Werrett, J. Scott, D. Tree, L. Baxter, Particle surface temperature measurements with multicolor band pyrometry, AIChE J. 55 (2009) 243–255.
[24] A. Macek, C. Bulik, Direct measurement of char-particle temperatures in fluidized-bed combustors, Proc. Combust. Inst. 20 (1984) 1223–1230.
[25] P. Toth, T. Draper, A.B. Palotas, T.A. Ring, E.G. Eddings, Three-dimensional combined pyrometric sizing and velocimetry of combusting coal particles. II: Pyrometry, Appl. Opt. 54 (2015) 4916–4926.
[26] V.C. Raj, S.V. Prabhu, Measurement of surface temperature and emissivity of different materials by two-colour pyrometry, Rev. Sci. Instrum. 84 (2013).
[27] F. Zander, Surface temperature measurements in hypersonic testing using digital single-lens reflex cameras, J. Thermophys. Heat Transf. 30 (2016) 919–925.
[28] S. Deep, Y. Krishna, G. Jagadeesh, Temperature characterization of a radiating gas layer using digital-single-lens-reflex-camera-based two-color ratio pyrometry, Appl. Opt. 56 (2017) 8492–8500.
[29] J.L. Urban, A.C. Fernandez-Pello, M. Vicariotto, D. Dunn-Rankin, Temperature measurement of glowing embers with color pyrometry, Fire Technol. (2019), https://doi.org/10.1007/s10694-018-0810-3.
[30] Y. Liu, J.L. Urban, C. Xu, C. Fernandez-Pello, Temperature and motion tracking of metal spark sprays, Fire Technol. (2019), https://doi.org/10.1007/s10694-019-00847-3.
[31] ASTM, ASTM D4442-16, Standard Test Methods for Direct Moisture Content Measurement of Wood and Wood-Based Materials, American Society of Testing and Materials, West Conshohocken, PA, 2016.
[32] J. Gabitto, C. Tsouris, Drag coefficient and settling velocity for particles of cylindrical shape, Powder Technol. 183 (2008) 314–322.
[33] P.B. Kuhn, B. Ma, B.C. Connelly, M.D. Smooke, M.B. Long, Soot and thin-filament pyrometry using a color digital camera, Proc. Combust. Inst. 33 (2011) 743–750.
[34] C. Mauer, Measurement of the Spectral Response of Digital Cameras with a Set of Interference Filters, Thesis Univ. of Applied Sciences Cologne, Dept. of Media- and Phototechnology, 2009.
[35] D. Coffin, Decoding Raw Digital Photos in Linux, (2018) https://www.cybercom.net/~dcoffin/dcraw/.
[36] D. De Sousa Meneses, P. Melin, L. del Campo, L. Cosson, P. Echegut, Apparatus for measuring the emittance of materials from far infrared to visible wavelengths in extreme conditions of temperature, Infrared Phys. Technol. 69 (2015) 96–101.
[37] Y. Xu, S. Li, Y. Yuan, Q. Yao, Measurement on the surface temperature of dispersed chars in a flat-flame burner using modified RGB pyrometry, Energy Fuels 31 (2017) 2228–2235.
[38] R.J. Jacob, D.J. Kline, M.R. Zachariah, High speed 2-dimensional temperature measurements of nanothermite composites: probing thermal vs. gas generation effects, J. Appl. Phys. 123 (2018) 115902.
[39] W. Tu, J. Lin, Y. Wu, An analysis of extinction coefficients of particles and water moisture in the stack after flue gas desulfurization at a coal-fired power plant, J. Air Waste Manag. Assoc. 61 (2011) 815–825.
[40] M.K. Misra, K.W. Ragland, A.J. Baker, Wood ash composition as a function of furnace temperature, Biomass Bioenergy 4 (1993) 103–116.